Geophysical Journal International

Geophys. J. Int. (2013) **194,** 1778–1788
Advance Access publication 2013 June 11

doi: 10.1093/gji/ggt190

Seismic waveform simulation with pseudo-orthogonal grids for irregular topographic models

Ying Rao[1,2] and Yanghua Wang[2]

[1]*State Key Laboratory of Petroleum Resources & Prospecting, China University of Petroleum (Beijing), China. E-mail: raoying@cup.edu.cn*
[2]*Department of Earth Science and Engineering, Centre for Reservoir Geophysics, Imperial College London, UK.*

Accepted 2013 May 8. Received 2013 May 7; in original form 2012 October 26

SUMMARY

In seismic waveform simulation, an irregular topography such as mountainous areas cannot be simplified to a flat surface. Even for marine seismic, a rough water bottom cannot be treated as a planar interface numerically. A body-fitted grid scheme will accurately present an earth model with an irregular topography. As it is a structured grid, then a simple finite difference scheme can be used as an efficient solver for waveform simulation. The pseudo-orthogonal property of grids is obtained by solving Poisson's equation. Investigation reveals that grids should have the acute angles $>67^\circ$ (90° for completely orthogonal) and the cell-size change rate <5 per cent, so that meshes are in a good orthogonality suitable for finite difference operation in waveform modelling. The acoustic wave equation and the absorbing boundary condition are reformulated from the physical space to the computational space. Waveform simulation and eventually tomographic inversion using a realistically complicated velocity model with a curved surface demonstrate the effectiveness of developed technology that works for irregular topographic models.

Key words: Numerical solutions; Tomography; Seismic tomography; Computational seismology; Wave propagation.

GJI Seismology

1 INTRODUCTION

Seismic waveform tomography has extensive development in last two decades (Pratt & Worthington 1990; Pratt *et al.* 1996; Ravaut *et al.* 2004; Operto *et al.* 2006; Bleibinhaus *et al.* 2007; Brenders & Pratt 2007; Wang & Rao 2009; Wang 2011). It can produce high-resolution image of subsurface velocity model with intense spatial variation. However, a flat surface is assumed in most previous works. In practice, especially for land seismic data, the irregular surface such as mountainous areas cannot be simplified to a flat line at all. Even for marine seismic data, a rough water bottom cannot be treated as a planar interface. Therefore, it is necessary to develop seismic waveform simulation methods, which works for models with irregular topography.

The procedure of tomographic inversion is to minimize iteratively the difference between observed and modelled wavefield (Pratt & Shipp 1999; Tarantola 2005; Wang & Rao 2006; Wang 2011), and an efficient and effective waveform simulation is critical for iteration. Among many existing technologies, finite difference method is often used for its efficiency and simple implementation (Liu *et al.* 2011; Virieux *et al.* 2011). In conventional finite difference method, a model is partitioned by quadrate cells with four sides perpendicular and parallel to the horizontal and vertical axis in the Cartesian coordinate, respectively. For irregular topography, the quadrate grids will form a staircase boundary which will cause strong artificial scattering numerically (Bleibinhaus & Rondenay 2009). Dense grids might have some degree of improvement (Lombard *et al.* 2008), but such an expensive approach cannot suppress numerical artefacts down to a satisfactory level.

Finite element method is a suitable method for seismic modelling, as triangular grids can well describe an irregular topography (Zhang & Liu 1999; Zhang 2004; Zhang & Gao 2011). This method is computationally expensive, in comparison to a finite difference method. Käser & Igel (2001) tried triangular grids in combination with finite difference for simulation. The errors in spatial derivative computations on unstructured grids were counteracted by using grids of higher node density. Thus, it also increased computational expense.

A curvilinear coordinate can be used to deal with irregular topography. In curved grids, horizontal lines coincide with the interfaces and the rows are still parallel to the vertical direction. An initial Cartesian model is transformed into a new computing model with a flat topography. The simulation is implemented in the curvilinear coordinate, using optimized operator of spatial derivatives (Hestholm & Ruud 1998, 2000; Tarrass *et al.* 2011). Whereas this method well describes an irregular topography, it needs compute more derivatives and thus is more than a Cartesian method (Komatitsch *et al.* 1996).

Body-fitted grid is a structured grid method, often used in hydrokinetics numerical simulation (Komatitsch *et al.* 1996). It is also

© The Authors 2013. Published by Oxford University Press on behalf of The Royal Astronomical Society.

Downloaded from http://gji.oxfordjournals.org/ at Imperial College London Library on January 17, 2014

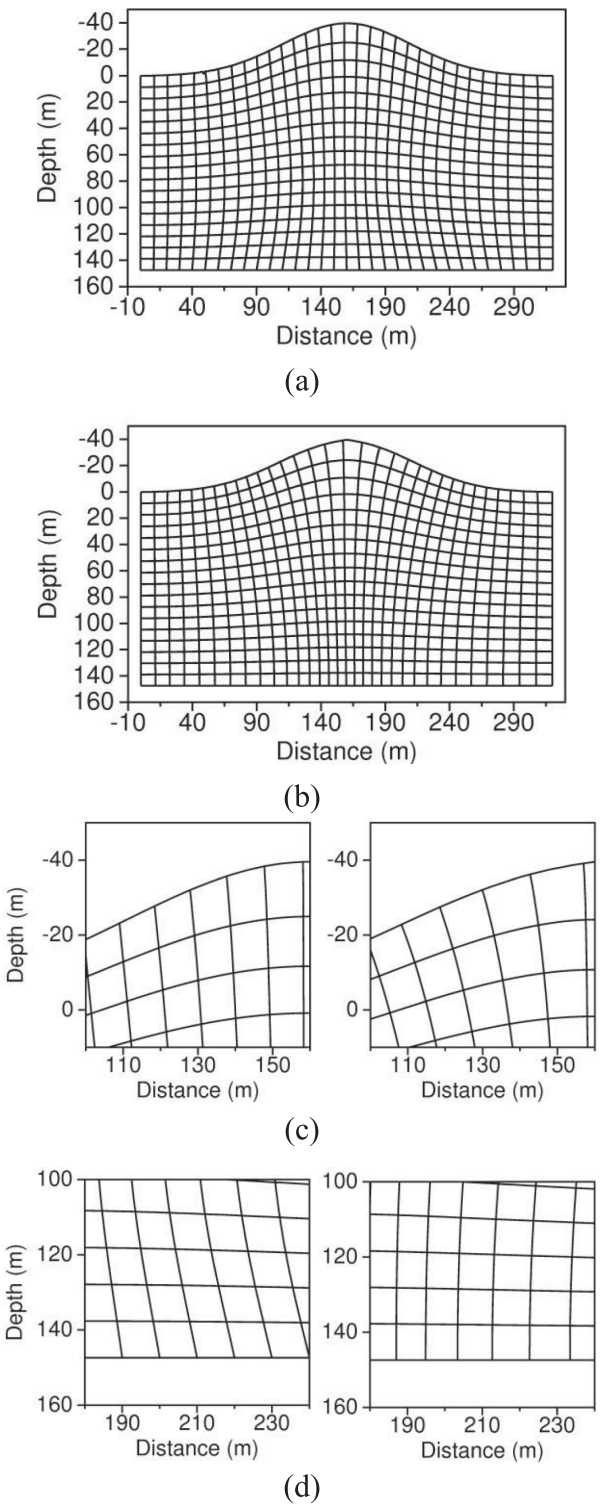


Figure 1. (a) Body-fitted grids (without boundary-point modification). (b) Body-fitted grids with boundary-point modification. (c) Zoomed-in meshes of (a) and (b) between $x = [100, 160]$ and $z = [-10, -50]$ m. (d) Zoomed-in meshes of (a) and (b) between $x = [180, 240]$ and $z = [100, 160]$ m. Because of boundary-point modification, both boundary and internal grids have a better orthogonal performance.

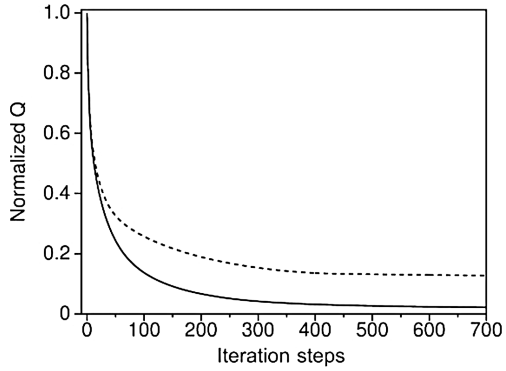


Figure 2. Grid quality parameter (normalized Q) versus the number of iterations. After boundary-point modification (solid curve), the quality parameter has quick convergence (towards zero) than that without modification (dashed curve).

a curved grid method producing pseudo-orthogonal meshes. Grids are quadrangle and, as structured, keep the similar neighbourhood relationships as they in Cartesian coordinate. By mapping curved grids onto rectangular grids in computational space, a simple finite difference scheme can be adopted straightforwardly.

Simple body-fitted grids can be generated by interpolation, which is an efficient method but strongly relies on the initial control points in the boundary (Komatitsch *et al.* 1996). The surface curve is represented by a polynomial, and any singular cells generated otherwise will crush computation. Zhang & Chen (2006) used a finite element software to generate body-fitted grids, for finite difference modelling. On other hand, Thomas & Middlecoeff (1980), Thompson *et al.* (1985) and Hoffman & Chiang (2000) presented a sophistic method that solves a hyperbolic system of equations with appropriate control functions. Because of improved orthogonality and smoothness with this grid method, numerical diffusion can be reduced and better accuracy is achieved in waveform simulation.

In this paper, we set up reliable initial mashes by linear interpolation and then generate body-fitted grids by solving a hyperbolic system of equations. As a research area is encircled by numerical boundaries, we modify points in four-side boundaries and connection zones, and manage to improve the orthogonality dramatically. Based on these structured grids, we reformulate the acoustic wave equation and the perfectly matched layer (PML) boundary condition in the computational space, and implement waveform simulation in the frequency domain using a finite difference scheme. After detailed investigation on the influence of orthogonality, skewness and cell-size change rate, etc. in seismic wavefields, we test the effectiveness of developed methodology using a realistically complicated velocity model with irregular surface, and demonstrate its potential in waveform simulation and inversion for irregular topographic models.

2 BODY-FITTED GRID GENERATION

Given a model in the physical space with coordinates (x, y), computation is implemented in a space with coordinates (ε, η). The relation between the physical space and the computational space is

Downloaded from http://gji.oxfordjournals.org/ at Imperial College London Library on Ja 14

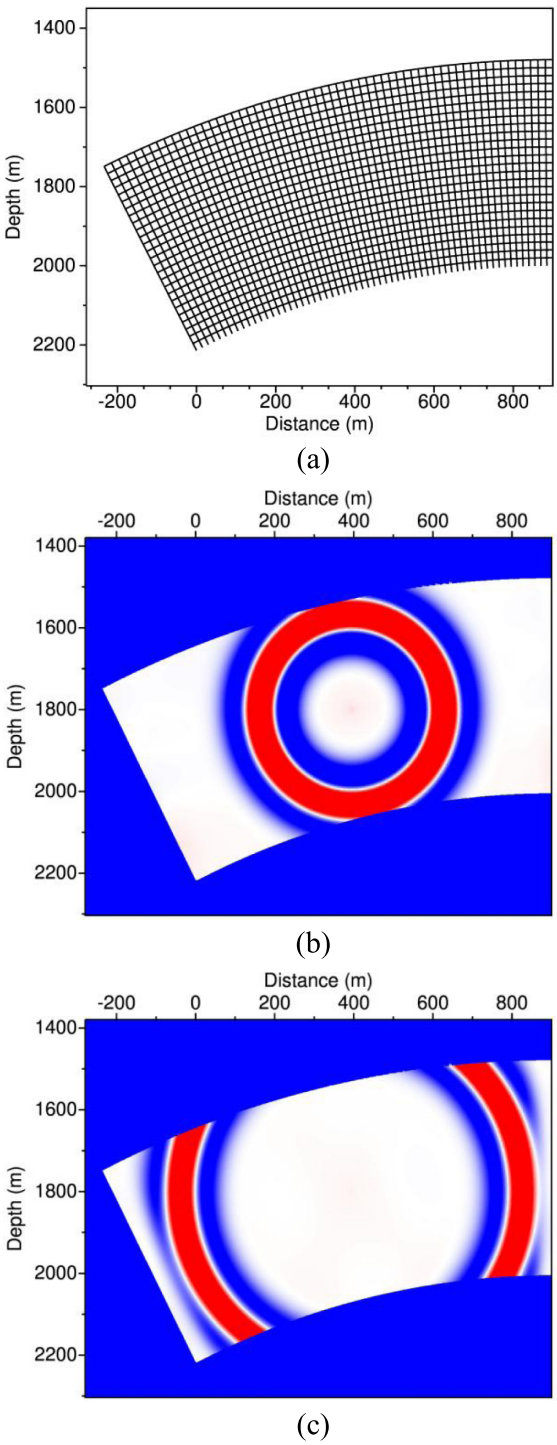


Figure 3. Seismic wave simulation in a homogeneous fan area. (a) The orthogonal meshes to partition the study area, plotted by each 5 grids. (b-c) Snapshots at a time 80 and 120 ms, respectively.

given by the following Poisson's equation (Thomas & Middlecoeff 1980):

$$\begin{cases} \dfrac{\partial^2 \varepsilon}{\partial x^2} + \dfrac{\partial^2 \varepsilon}{\partial z^2} = M(\varepsilon, \eta), \\ \dfrac{\partial^2 \eta}{\partial x^2} + \dfrac{\partial^2 \eta}{\partial z^2} = N(\varepsilon, \eta), \end{cases} \tag{1}$$

where $M(\varepsilon, \eta)$ and $N(\varepsilon, \eta)$ are two terms controlling the rate of grid spacing changes in both directions (Appendix A). To find the physical space coordinates $x = x(\varepsilon, \eta)$ and $y = y(\varepsilon, \eta)$ corresponding to any rectangular cells in the computational space, eq. (1) may be transferred to

$$\begin{cases} \alpha \dfrac{\partial^2 x}{\partial \varepsilon^2} - 2\beta \dfrac{\partial^2 x}{\partial \varepsilon \partial \eta} + \gamma \dfrac{\partial^2 x}{\partial \eta^2} + J^2 \left(M \dfrac{\partial x}{\partial \varepsilon} + N \dfrac{\partial x}{\partial \eta} \right) = 0, \\ \alpha \dfrac{\partial^2 z}{\partial \varepsilon^2} - 2\beta \dfrac{\partial^2 z}{\partial \varepsilon \partial \eta} + \gamma \dfrac{\partial^2 z}{\partial \eta^2} + J^2 \left(M \dfrac{\partial z}{\partial \varepsilon} + N \dfrac{\partial z}{\partial \eta} \right) = 0, \end{cases} \tag{2}$$

where

$$\alpha = \dot{x}_\eta^2 + \dot{z}_\eta^2, \quad \beta = \dot{x}_\varepsilon \dot{x}_\eta + \dot{z}_\varepsilon \dot{z}_\eta, \quad \gamma = \dot{x}_\varepsilon^2 + \dot{z}_\varepsilon^2,$$

$$J \equiv \frac{\partial(x, z)}{\partial(\varepsilon, \eta)} = \dot{x}_\varepsilon \dot{z}_\eta - \dot{z}_\varepsilon \dot{x}_\eta.$$

In an Successive-Over-Relaxation approach to solve discretized Poisson's equation, $\dot{x}_\varepsilon = \partial x / \partial \varepsilon$, $\dot{z}_\varepsilon = \partial z / \partial \varepsilon$, $\dot{x}_\eta = \partial x / \partial \eta$, $\dot{z}_\eta = \partial z / \partial \eta$ are assumed to be known parameters, evaluated based on current solution.

Any grid points should satisfy the following orthogonality condition:

$$\beta = \dot{x}_\varepsilon \dot{x}_\eta + \dot{z}_\varepsilon \dot{z}_\eta = 0. \tag{3}$$

Therefore, a measurement for the quality of computational grids is

$$Q = \sum_{i,j} \beta, \tag{4}$$

where (i, j) are indexes of grids. A small Q value means a better orthogonality of meshes and ideally, $Q = 0$.

Solving Poisson's eq. (2) generates interior grids which usually have excellent spatial distribution. However, grids at boundaries are not orthogonal, and we need to modify the position of boundary points (Patantonis & Atharassiadis 1985), following the pragmatic rule $\beta = 0$ in eq. (3). Meanwhile, the smoothness in both ε and η-directions should be also considered after boundary-point modification. While orthogonality in boundary grids is necessary for properly setting any absorbing boundary condition for waveform simulation, smoothness is critical to the accuracy of waveform simulation. Therefore, a modified boundary point should satisfy the following system of three equationsas

$$\begin{cases} (x_{i+1,j} - x_{i-1,j})(\tilde{x}_{i,j+1} - x_{i,j}) + (z_{i+1,j} - z_{i-1,j}) \\ \qquad \times (\tilde{z}_{i,j+1} - z_{i,j}) = 0, \\ (x_{i+1,j+1} - \tilde{x}_{i,j+1})(\tilde{z}_{i,j+1} - z_{i-1,j+1}) - (\tilde{x}_{i,j+1} - x_{i-1,j+1}) \\ \qquad \times (z_{i+1,j+1} - \tilde{z}_{i,j+1}) = 0, \\ (x_{i,j+2} - \tilde{x}_{i,j+1})(\tilde{z}_{i,j+1} - z_{i,j}) - (\tilde{x}_{i,j+1} - x_{i,j}) \\ \qquad \times (z_{i,j+2} - \tilde{z}_{i,j+1}) = 0. \end{cases} \tag{5}$$

This system modifies grid point $(i, j+1)$ from $(x_{i,j+1}, z_{i,j+1})$ to $(\tilde{x}_{i,j+1}, \tilde{z}_{i,j+1})$. The first equation is from the orthogonality eq. (3), and the rest represent the smoothness in ε and η-directions at $(x_{i,j+1}, z_{i,j+1})$, respectively. In practice, the modification can be compromised by $\hat{x}_{i,j+1} = (w\tilde{x}_{i,j+1} + x_{i,j+1})/(1 + w)$ and $\hat{z}_{i,j+1} = (w\tilde{z}_{i,j+1} + \tilde{z}_{i,j+1})/(1 + w)$, where w is a parameter set to keep it smooth enough after modification.

Downloaded from http://gji.oxfordjournals.org/ at Imperial College London Library on January 17, 2014

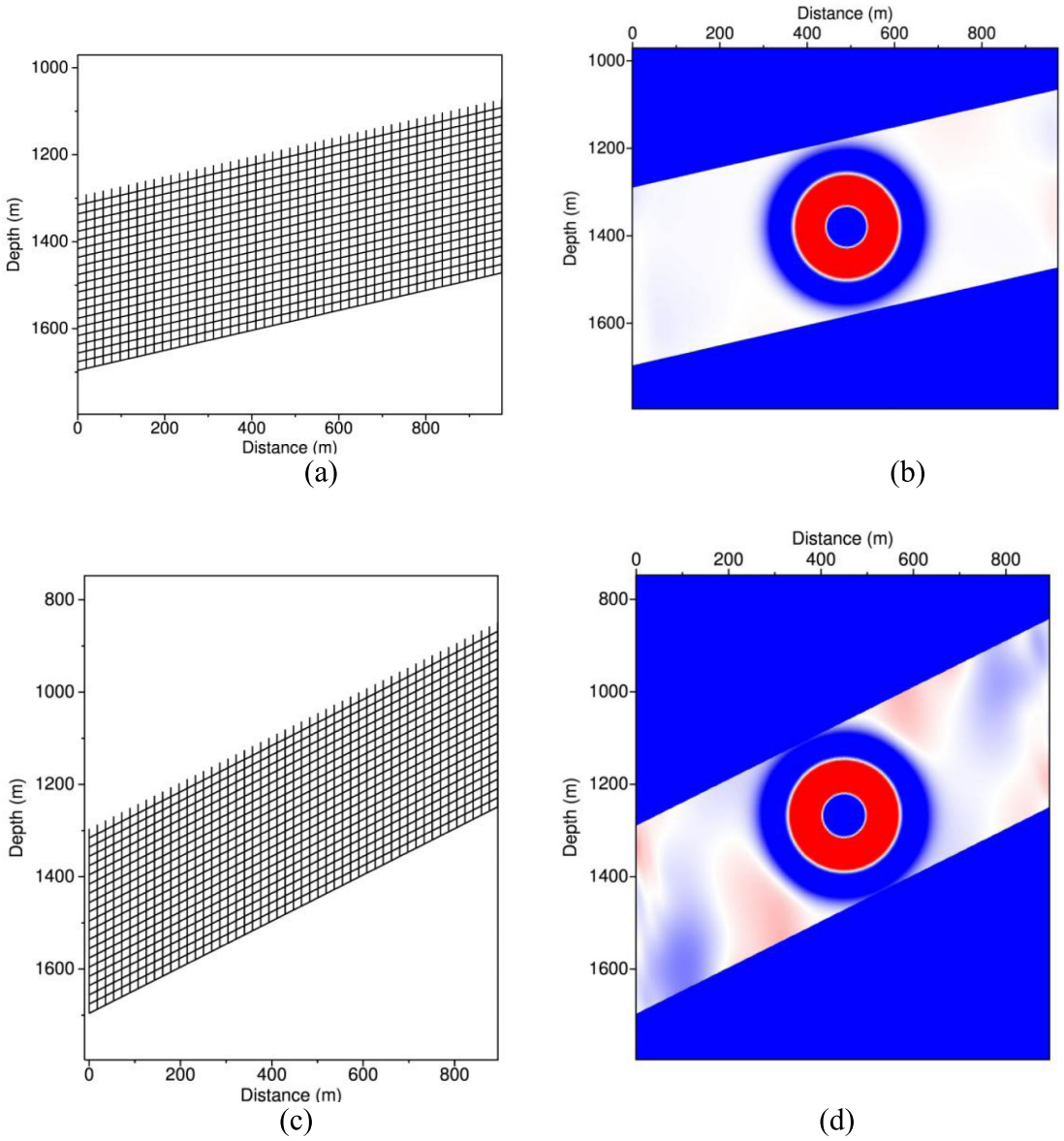


Figure 4. Seismic wave simulation in a homogeneous area, using parallelogram grid. (a) Parallelogram grids with an acute angle 77.1°. (b) Snapshot of wave propagation at 50 ms. (c) Parallelogram grids with an acute angle 63.5°. (d) Snapshot of wave propagation at 50 ms.

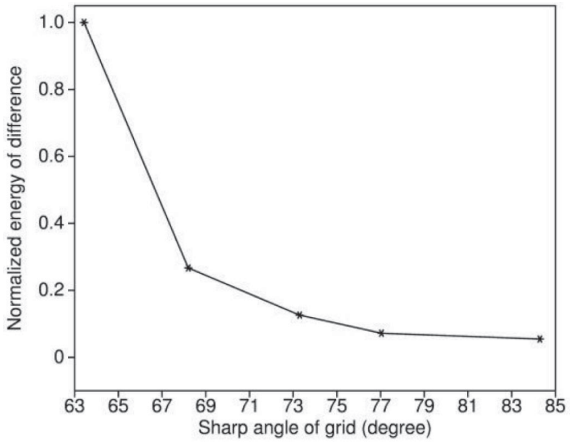


Figure 5. Normalized energy of background noise, when wavefield simulation using parallelogram grids with different acute angles.

In seismic waveform simulation, we set $M(\varepsilon, \eta) = 0$, and evaluate $N(\varepsilon, \eta)$ in the depth direction, so that the grid can be sparse in the deep area with high velocity and be tight in the shallow area with low velocity. Associating with a general trend of velocity variation in depth, a grid size can be changed from r to $r + \mathrm{d}r$. The controlling term is evaluated by

$$N(\varepsilon, \eta) = \frac{-2L(\alpha + \gamma)\mathrm{d}r}{J^2 \dot{z}_\eta (1 + r)^2}, \tag{6}$$

where $L = z_{i,j+1} - z_{i,j-1}$ is the closest distance in the η-direction between two points next to point $z_{i,j}$ (Appendix A).

In summary, the procedure for generating body-fitted grids consists of the following steps:

(1) Setting evenly spaced initial points on four boundaries.
(2) Generating initial internal grids by linear interpolation over those initial points on boundaries.

Downloaded from http://gji.oxfordjournals.org/ at Imperial College London Library on Ja 14

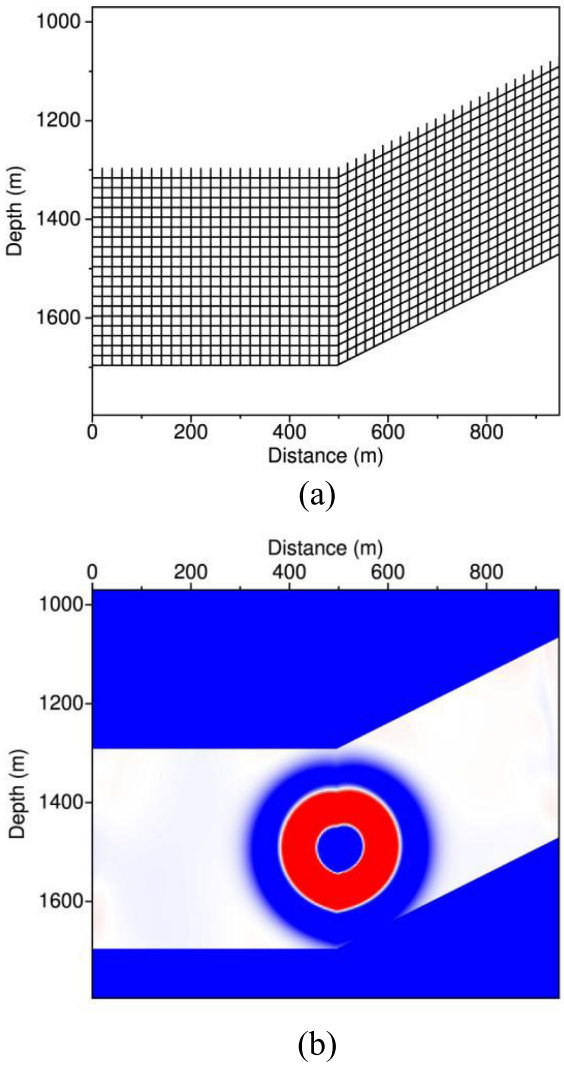


Figure 6. Wavefield simulation in a homogeneous area with a skewness. (a) The meshes to partition the area. (b) A snapshot at 50 ms, showing twisted wave front because of the skewness of meshes.

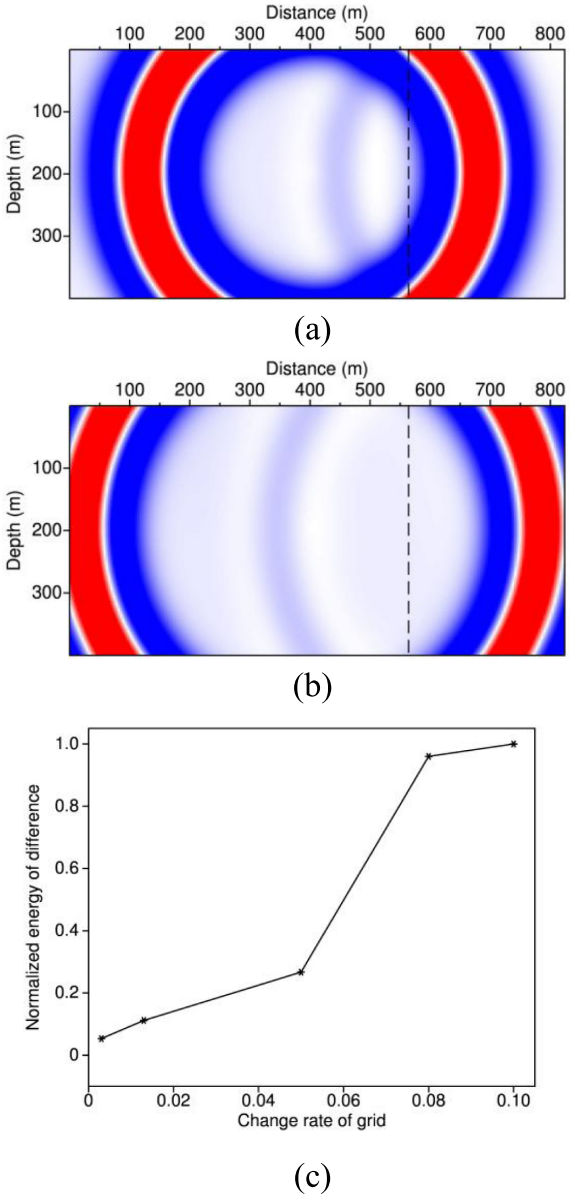


Figure 7. Wavefield simulation in a homogeneous area. At marked (in dash line) distance 564 m, the grid interval at the right-hand side is 4.4 m, and at the left-hand side is 4 m. So the change rate is 10 per cent. (a and b) Snapshots at 90 and 110 ms, respectively. (c) Normalized energy of reflection caused by different change rate of grids.

(3) Solving Poisson's equation for orthogonal internal meshes.
(4) Modifying boundary points.
(5) Measuring quality of grids.
(6) Adjusting $M(\varepsilon, \eta)$ and $N(\varepsilon, \eta)$, and going to step 3 to repeat the computation.

The iteration is stopped until the Q value is sufficiently small.

3 ORTHOGONALITY, SKEWNESS AND GRID-SIZE CHANGES

Fig. 1 is a simple example in which the bottom boundary and the left and right boundaries are planar, but the top topography is an analytical curve, $40\exp[-(x-160)^2/100^2]$, where x is the lateral coordinate.

In body-fitted grids generated from Poisson's equation, most internal meshes are orthogonal, except of near-boundary zones (Fig. 1a). These unorthogonal meshes will twist calculated wavefield. Therefore, boundary points are modified in the iterative mesh generation procedure. The resultant meshes show smooth and orthogonal characters in both internal and boundary grids (Fig. 1b). Fig. 1(c) is zoomed-in pictures of the top boundary at range $x = [100, 160]$ m and $z = [-10, -50]$ m, corresponding to two cases before and after boundary-point modification. Fig. 1(d) is zoomed-in pictures of the bottom boundary at $x = [180, 240]$ and $z = [100, 160]$ m.

Fig. 2 displays a quality measurement, normalized Q, versus iterations. The curve without boundary-point modification is plotted in dash line. The curve after boundary-point modification within each iteration is plotted in solid line. Comparison reveals that modification can make a quick convergence. It also means that meshes have a better orthogonal behaviour that suits for finite difference calculation.

Downloaded from http://gji.oxfordjournals.org/ at Imperial College London Library on January 17, 2014

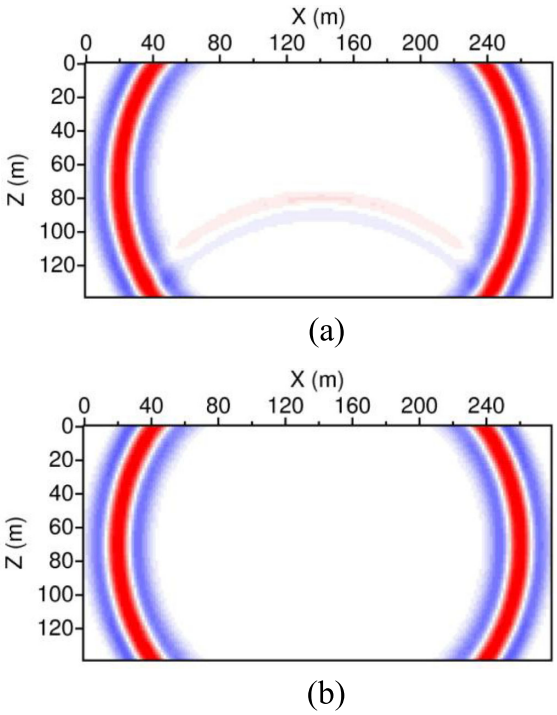


Figure 8. The snapshot at 50 ms. (a) At the bottom boundary, a paraxial approximation boundary condition is used. (b) At the bottom boundary, the PML boundary condition is used. For the rest three boundaries, the PML method is used.

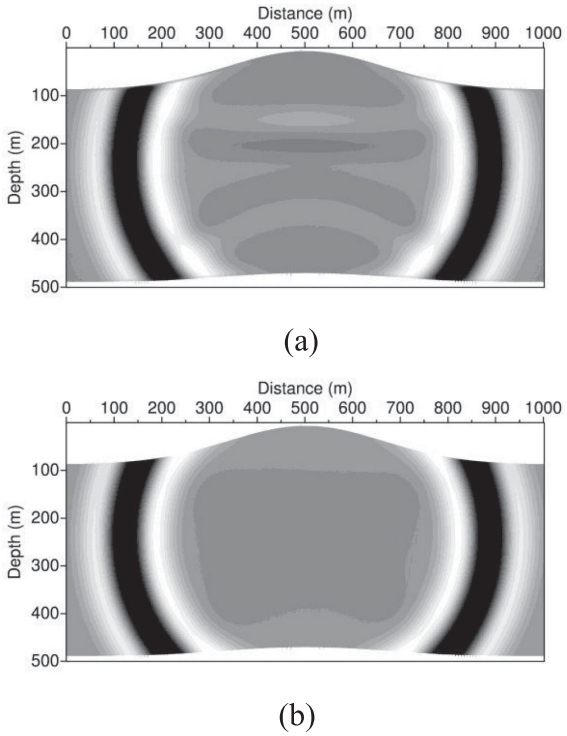


Figure 9. The snapshots at 110 ms. (a) At irregular topography boundaries, a paraxial approximation boundary condition is used. (b) At irregular topography boundaries, PML boundary condition is used.

Fig. 3(a) is a simple curvilinear grid to partition a fan area. As the topography is defined by circular-arc function, it can form ideal curvilinear orthogonal meshes. While one dimension of the meshes coincides with the topography, the other dimension is along the normal line to the topography. Figs 3(b) and (c) are the snapshots of seismic wavefield at time 80 and 120 ms, respectively. These curvilinear orthogonal meshes show excellent performance in wavefield simulation by a finite difference method. For the real situation, however, the topography is often too complex to form completely orthogonal meshes. Body-fitted grid method can be an alternative to build pseudo-orthogonal meshes.

To test the effect of skewness in wavefield simulation, Fig. 4 compares two meshes with skewangle of 77.1° and 63.5°, respectively (Figs 4a and c). Snapshots at 50 ms propagation time clearly indicate that wavefield modelling in meshes with 77.1° skewangle (Fig. 4b) has better performance in accuracy than that with 63.5° skewangle (Fig. 4d). Both use the same second-order finite difference operator. Performance is quantified by normalized energy of difference between theoretical and simulated wavefield, using parallelogram grid with different acute angle (Fig. 5). For example, when using meshes with 67° skewangle, the energy of difference in wavefield is 75 per cent less than that with 63° skewangle. When the skewangle close to 90° (completely orthogonal), the accuracy of wavefield modelling will be improved ultimately.

Fig. 6 demonstrates the importance of smoothness in curved meshes. Because of a skewness of meshes (Fig. 6a), snapshot at 50 ms propagation time (Fig. 6b) shows twisted wave front correspondingly. Fortunately, meshes generated by Poisson's equation have enough smoothness and do not show any of this kind sudden skewness.

The change rate in cell size is another critical aspect to determine the accuracy of finite difference wavefield modelling. Figs 7(a) and (b) show two snapshots at 90 and 110 ms, respectively. At marked distance (hashed line in 564 m), the horizontal grid interval is 4 m at the left-hand side and 4.4 m at the right-hand side. Snapshots indicate that such a 10 per cent cell-size change can act as an artificial reflection boundary in homogeneous media. Fig. 7(c) is normalized energy of artificial reflection, caused by different change rate of cell size. When the change rate is less than 5 per cent, normalized energy of artificial reflection reduces to 20 per cent of that with 8–10 per cent change rate.

In general, for pseudo-orthogonal grids being applicable to waveform simulation, the acute angle should be controlled in a range between 67° and 90°, and grid-size change rate should be <5 per cent. These targets can be achieved by adjusting terms M and N in Poisson's eq. (2).

4 WAVE EQUATION AND ABSORBING BOUNDARY CONDITION

Based on the relation between computational coordinates (ε, η) and physical coordinates (x, y), the first-order differentiation is

$$\frac{\partial P}{\partial x} = \varepsilon_x \frac{\partial P}{\partial \varepsilon} + \eta_x \frac{\partial P}{\partial \eta}$$

and the second-order differentiation is

$$\frac{\partial^2 P}{\partial x^2} = \dot{\varepsilon}_x^2 \frac{\partial^2 P}{\partial \varepsilon^2} + \dot{\eta}_x^2 \frac{\partial^2 P}{\partial \eta^2} + 2\dot{\varepsilon}_x \dot{\eta}_x \frac{\partial^2 P}{\partial \varepsilon \partial \eta} + \ddot{\varepsilon}_{xx} \frac{\partial P}{\partial \varepsilon} + \ddot{\eta}_{xx} \frac{\partial P}{\partial \eta}.$$

Downloaded from http://gji.oxfordjournals.org/ at Imperial College London Library on Ja 14

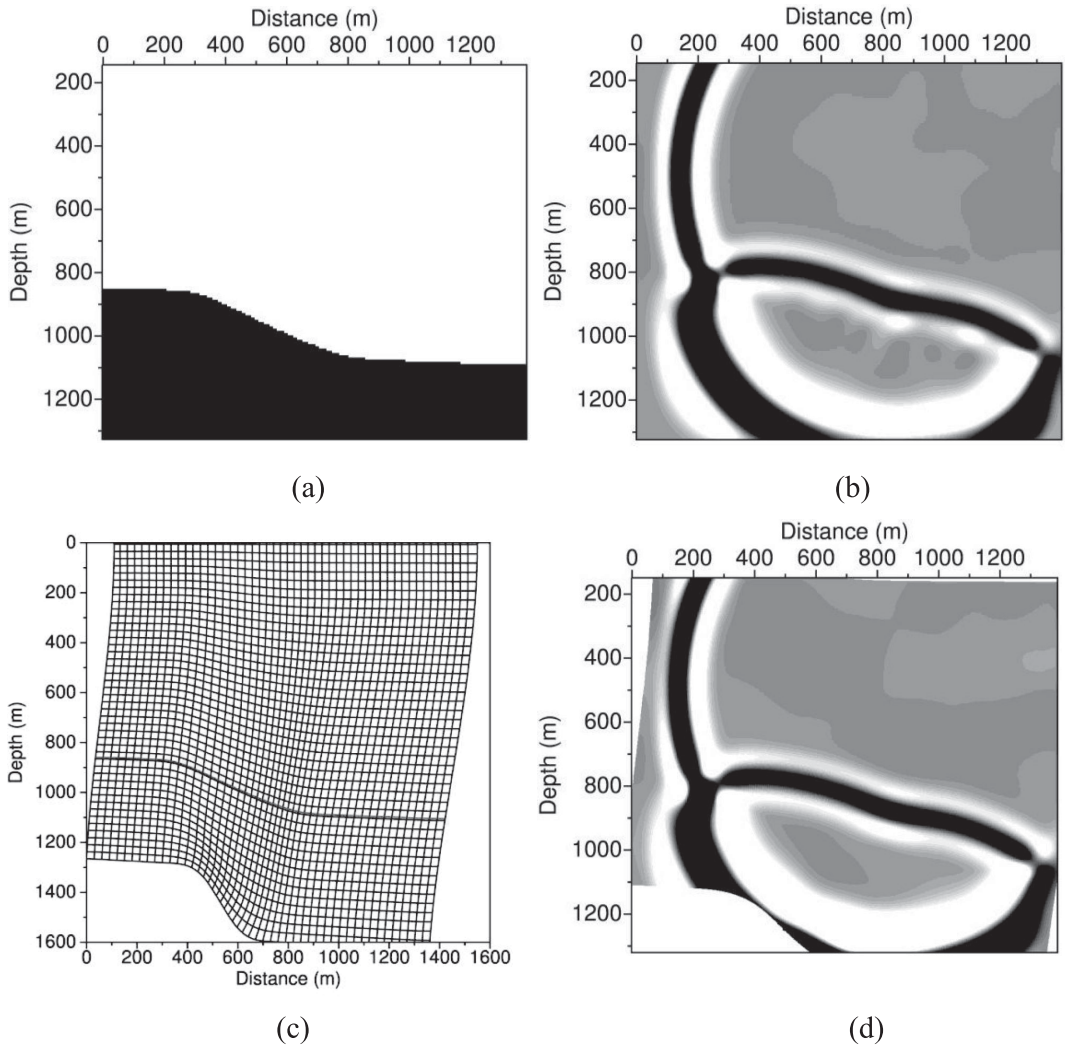


Figure 10. (a) Velocity model with staircase boundary, caused by quadrate grids partition at a dip subsurface boundary. (b) The snapshot at 190 ms, showing that the staircase boundary could cause strong scattering effect in the wavefield. (c) Pseudo-orthogonal grid for the same area, where the red line is the subsurface boundary. (d) The corresponding snapshot at 190 ms without scattering effect, when using pseudo-orthogonal grid.

The acoustic wave equation in computational space may be presented as

$$\left(\dot{\varepsilon}_x^2+\dot{\varepsilon}_z^2\right)\frac{\partial^2 P}{\partial \varepsilon^2}+\left(\dot{\eta}_x^2+\dot{\eta}_z^2\right)\frac{\partial^2 P}{\partial \eta^2}+2\left(\dot{\varepsilon}_x\dot{\eta}_x+\dot{\varepsilon}_z\dot{\eta}_z\right)\frac{\partial^2 P}{\partial \varepsilon\partial \eta}$$
$$+\left(\ddot{\varepsilon}_{xx}+\ddot{\varepsilon}_{zz}\right)\frac{\partial P}{\partial \varepsilon}+\left(\ddot{\eta}_{xx}+\ddot{\eta}_{zz}\right)\frac{\partial P}{\partial \eta}+\frac{\omega^2}{v^2}P=0. \qquad (7)$$

For 3-D case, see Appendix B.

Then a proper absorbing boundary condition is critical in cases with an irregular topography, as a small incidence angle in a flat boundary could be a big angle in an irregular boundary. Consider a plane wave as

$$u=u_0\exp\left[\mathrm{i}(\omega t-k_x x)\right], \qquad (8)$$

where t is traveltime, ω is the angular frequency and k_x is the wavenumber in x-direction. The aim of an absorbing boundary in the numerical computation is to modify the wave solution such that the amplitude is attenuated to

$$\tilde{u}=u\exp\left[-\alpha x\right], \qquad (9)$$

where α is an attenuation coefficient and is chosen such that $\mathrm{e}^{-\alpha x}\big|_{x=0}=1$ and $\mathrm{e}^{-\alpha x}\big|_{x>0}<1$. That is, at position $x=0$ the solution is perfectly matched (before finite difference approximation) and will not cause any reflection. This is the PML method, developed first for electromagnetic waves (Bérenger 1994, 1996). To understand the concept, we put it in the context of acoustic wave propagation, and reformulate it for cases with an irregular topography in the computational space.

Defining the attenuation coefficient as a frequency-dependent function

$$\alpha x=\frac{k_x}{\omega}\int_0^x d(\ell)\mathrm{d}\ell, \qquad (10)$$

where $d(x)$ is a damping factor within the PML region. Then

$$\begin{aligned}\tilde{u}&=u_0\exp\left[\mathrm{i}\left(\omega t-(k_x-\mathrm{i}\alpha)x\right)\right]\\&=u_0\exp\left[\mathrm{i}\left(\omega t-k_x\left(x+\frac{1}{\mathrm{i}\omega}\int_0^x d(\ell)\mathrm{d}\ell\right)\right)\right]\\&=u_0\exp\left[\mathrm{i}\left(\omega t-k_x\tilde{x}\right)\right],\end{aligned} \qquad (11)$$

Downloaded from http://gji.oxfordjournals.org/ at Imperial College London Library on January 17, 2014

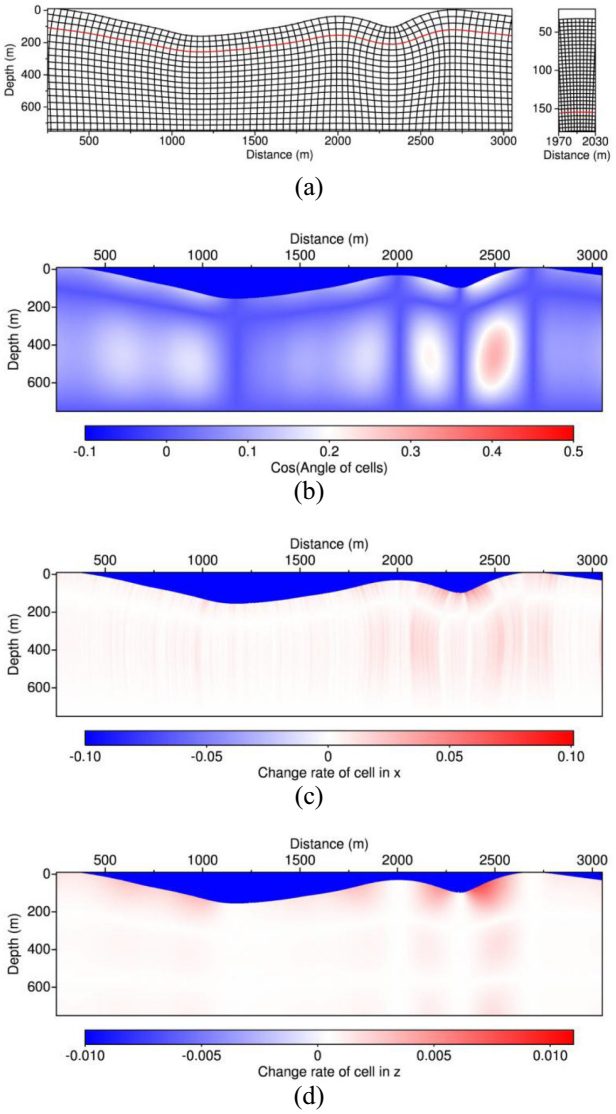


Figure 11. (a) Body-fitted grids and zoomed-in meshes. The top surface is plotted in red curve, above which are the grids for PML boundary condition. (b) Cosine values of the acute angles in grids. (c) Change rates of grid interval in x-direction. (d) Change rates of grid interval in z-direction.

where

$$\tilde{x} = x + \frac{1}{\mathrm{i}\omega}\int_0^x d(\ell)\mathrm{d}\ell. \tag{12}$$

Therefore, PML involves the change of a real-valued spatial variable x to a complex-valued variable $\tilde{x}$, as defined by eq. (12).

Changing variable $x \to \tilde{x}$ is equivalently to the following change to partial differential:

$$\frac{\partial}{\partial x} \to \frac{1}{s_x}\frac{\partial}{\partial x}, \tag{13}$$

where s_x is a complex stretching factor, defined by

$$s_x \equiv \frac{\partial \tilde{x}}{\partial x} = 1 + \frac{\mathrm{d}(x)}{\mathrm{i}\omega} \tag{14}$$

following eq. (12).

To stretch the computational coordinates $\varepsilon \to \tilde{\varepsilon}$ and $\eta \to \tilde{\eta}$, partial differentials in eq. (7) are replaced as

$$\frac{\partial}{\partial \varepsilon} \to \frac{1}{s_\varepsilon}\frac{\partial}{\partial \varepsilon}, \quad \frac{\partial}{\partial \eta} \to \frac{1}{s_\eta}\frac{\partial}{\partial \eta}, \tag{15}$$

$$\frac{\partial^2}{\partial \varepsilon^2} \to \frac{\partial^2}{\partial \tilde{\varepsilon}^2} = \frac{1}{s^3(\varepsilon)}\frac{1}{\mathrm{i}\omega}\frac{\partial d(\varepsilon)}{\partial \varepsilon}\frac{\partial}{\partial \varepsilon} + \frac{1}{s^2(\varepsilon)}\frac{\partial^2}{\partial \varepsilon^2}, \tag{16}$$

$$\frac{\partial^2}{\partial \eta^2} \to \frac{\partial^2}{\partial \tilde{\eta}^2} = \frac{1}{s^3(\eta)}\frac{1}{\mathrm{i}\omega}\frac{\partial d(\eta)}{\partial \eta}\frac{\partial}{\partial \eta} + \frac{1}{s^2(\eta)}\frac{\partial^2}{\partial \eta^2}. \tag{17}$$

Then, the acoustic wave eq. (7) in absorbing zone is written as

$$\begin{aligned}&\frac{(\dot{\varepsilon}_x^2+\dot{\varepsilon}_z^2)}{\mathrm{i}\omega s^3(\varepsilon)}\frac{\partial d(\varepsilon)}{\partial \varepsilon}\frac{\partial P}{\partial \varepsilon} + \frac{(\dot{\varepsilon}_x^2+\dot{\varepsilon}_z^2)}{s^2(\varepsilon)}\frac{\partial^2 P}{\partial \varepsilon^2} + \frac{(\dot{\eta}_x^2+\dot{\eta}_z^2)}{\mathrm{i}\omega s^3(\eta)}\frac{\partial d(\eta)}{\partial \eta}\frac{\partial P}{\partial \eta}\\ &+ \frac{(\dot{\eta}_x^2+\dot{\eta}_z^2)}{s^2(\eta)}\frac{\partial^2 P}{\partial \eta^2} + 2(\dot{\varepsilon}_x\dot{\eta}_x+\dot{\varepsilon}_z\dot{\eta}_z)\frac{1}{s_\varepsilon s_\eta}\frac{\partial^2 P}{\partial \varepsilon \partial \eta} + \frac{(\ddot{\varepsilon}_{xx}+\ddot{\varepsilon}_{zz})}{s_\varepsilon}\frac{\partial P}{\partial \varepsilon}\\ &+ \frac{(\ddot{\eta}_{xx}+\ddot{\eta}_{zz})}{s_\eta}\frac{\partial P}{\partial \eta} + \frac{\omega^2}{v^2}P = 0.\end{aligned} \tag{18}$$

Fig. 8 compares two snapshots (at 50 ms) of simulated wavefield, using a paraxial approximation boundary condition (Clayton & Engquist 1977) and the PML boundary condition (18) at the flat bottom boundary. For the simplicity, the PML method is used for the rest three boundaries. The model velocity is 3000 m s^{-1}, and the grid size is 2 m. The artificial reflection from the bottom boundary when using a paraxial approximation boundary condition (Fig. 8a) has been effectively suppressed from the result of PML boundary condition (Fig. 8b).

In this example, the PML consists of 20 cells. The damping function within the PML region $x \in [0, L]$ is

$$d(x) = k\left[1 - \cos^2\left(\frac{\pi}{2}\frac{x}{L}\right)\right], \tag{19}$$

where $k = 3.6 \times 10^6\,(\omega/v)^2$ is a function of wavenumber (ω/v).

Fig. 9 is an example with two curved boundaries. Fig. 9(a) is a snapshot of wavefield from using a paraxial approximation boundary condition (Clayton & Engquist 1977). Fig. 9(b) is a result of PML boundary application. The latter has a much better wave-absorbing performance than the paraxial approximation boundary condition for irregular boundaries, as strong reflections from large incidence angles in Fig. 9(a) disappear from (b).

In conventional finite difference scheme using quadrate grids in the Cartesian coordinate, a 'staircase' boundary (Fig. 10a) will cause strong scattering in the wavefield (Fig. 10b). It can be improved by fine partitioning with increased computational expense. In contrast, when using pseudo-orthogonal grids for the same area (Fig. 10c), there is no extra computational expanse for describing the irregular boundary with finite differencing, and there is no artificial scattering effect (Fig. 10d). With pseudo-orthogonal grids, there is a simple relationship between grid connections and thus it is also easy to solve the boundary condition.

5 WAVEFORM SIMULATION AND INVERSION

To demonstrate the application, we carry out waveform simulation and ultimately tomographic inversion for a near-surface velocity model with irregular topography. The model size is 3050 × 650 m^2. The top boundary is an irregular surface, with the highest depth difference about 100 m. A line of sources and a line of receivers are

Downloaded from http://gji.oxfordjournals.org/ at Imperial College London Library on Ja 14

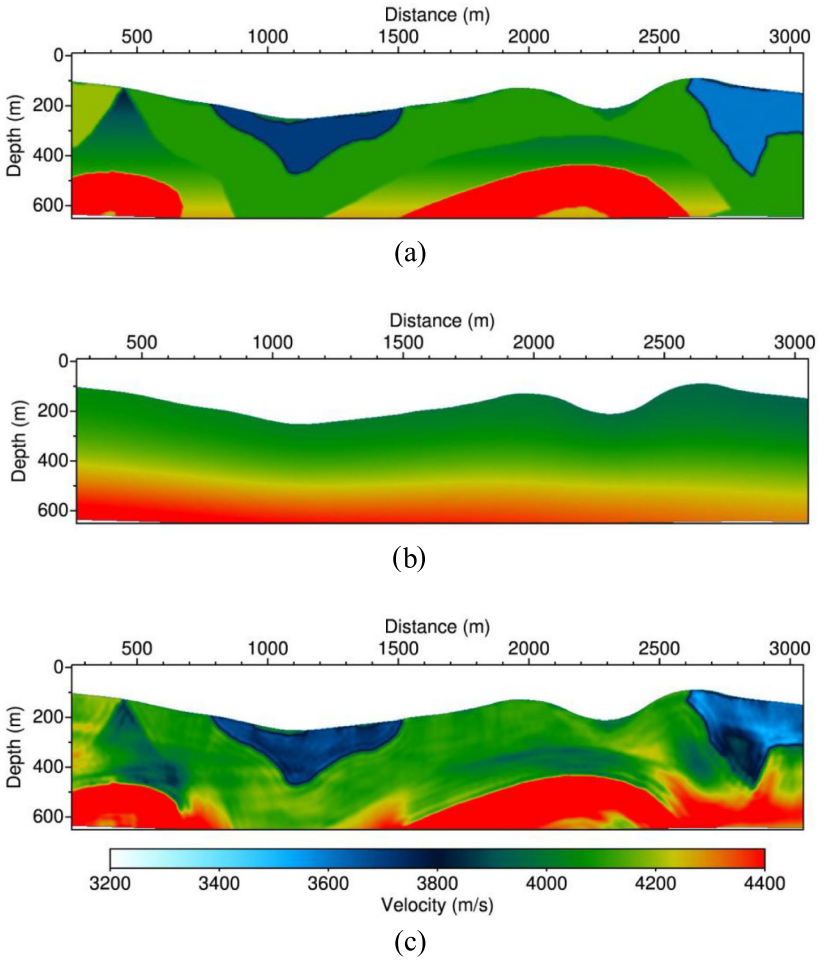


Figure 12. (a) A complicated velocity model with irregular topography. (b) The initial velocity model for waveform inversion. (c) Reconstructed velocity model generated by waveform tomography.

placed along the top boundary with 10-m interval in the horizontal direction.

Fig. 11(a) is sparsely sampled grids (left-hand side), but the actual grids have an average grid size of 5 m (right). The surface is plotted in red curve in both diagrams. All grids have a good smoothness and a good orthogonality, in both the artificial boundaries and the Earth surface. The quality is measured by the following three panels. Fig. 11(b) is the cosine values of acute angles in meshes. The acute angles vary between 75° and 90°. The grids closed to the top surface have better orthogonality after boundary-point modification. Figs 11(c) and (d) are change rates of grid size in x- and z-directions, respectively. The change rate in x-direction is <5 per cent, and the change rate in z-direction is <1 per cent. These quantitative measurements suggest a guaranteed accuracy of wavefield simulation with a finite difference method in the computational space.

Fig. 12(a) is the actual velocity model. We use the body-fitted grid method to partition this model into 670 × 150 grids, as shown in the previous figure. We generate synthetic wavefields using finite difference approximation to the acoustic wave equation and PML boundary condition in the computational space. The synthetic source is a Ricker wavelet with a 30-Hz dominant frequency.

For waveform tomography, we set an initial model in Fig. 12(b), which is a smoothed version of the true model. The inversion is implemented in the frequency domain. For the detailed procedure, please refer to Wang (2011). Reconstructed velocity model by waveform tomography is shown in Fig. 12(c). It clearly recovers main structures in the true model, especially the low-velocity structures with irregular triangle forms, both at the distance of 900–1700 m and the depth of 200–300 m, and the distance of 2700–3650 m and the depth of 100–500 m. The thin high-velocity layer on the top of a low-velocity structure has also been revealed. The keen-edge structures, at the distance of 550 and 2400 m, have been recovered as well.

For the calculation of forward modelling of a single frequency component, the running time is 0.8 min, with 0.376 GiB memory. For a single iteration of full waveform inversion with one frequency component, it costs 3.28 min for the calculation in a single CPU.

6 CONCLUSIONS

This paper has implemented a body-fitted grid method to accurately describe a model with an irregular topography. With this structured grid method, instead of an unstructured triangular grid, we are able to use a simple finite difference scheme, instead of a finite element method, as an efficient solver for waveform simulation.

The orthogonality of grids is obtained by solving Poisson's equation, with additional boundary-point modification. We have found that the acute angle should be $>67°$ and grid-size change should be <5 per cent in grid generation, so that meshes have a good quality and are suitable for second-order finite difference operation in waveform modelling.

Downloaded from http://gji.oxfordjournals.org/ at Imperial College London Library on January 17, 2014

We have also reformulated the acoustic wave equation and the PML absorbing boundary condition from the physical space to the computational space. We have demonstrated the effectiveness of developed technology in waveform simulation and eventually tomographic inversion, using a realistically complicated velocity model with curved topography.

ACKNOWLEDGEMENTS

The authors are grateful to the sponsors of the Centre for Reservoir Geophysics, Imperial College London, for supporting this research. YR also acknowledges the sponsors of National Natural Science Foundation of China (41104082 and U1262207) and Research Funds of China University of Petroleum-Beijing (QD-2011-01).

REFERENCES

Bérenger, J.P., 1994. A perfectly matched layer for the absorption of electromagnetic waves, *J. Comput. Phys.,* **114,** 185–200.

Bérenger, J.P., 1996. Three-dimensional perfectly matched layer for the absorption of electromagnetic waves, *J. Comput. Phys.,* **127,** 363–379.

Bleibinhaus, F. & Rondenay, S., 2009. Effects of surface scattering in full-waveform inversion, *Geophysics,* **74,** WCC69–WCC77.

Bleibinhaus, F., Hole, J.A., Ryberg, T. & Fuis, G.S., 2007. Structure of the California Coast Ranges and San Andreas Fault at SAFOD from seismic waveform inversion and reflection imaging, *J. geophys. Res.,* **112,** B06315, doi:10.1029/2006JB004611.

Brenders, A.J. & Pratt, R.G., 2007. Efficient waveform tomography for lithospheric imaging: implications for realistic, two-dimensional acquisition geometries and low-frequency data, *Geophys. J. Int.,* **168,** 152–170.

Clayton, R. & Engquist, B., 1977. Absorbing boundary conditions for acoustic and elastic wave equations, *Bull. seism. Soc. Am.,* **67,** 1529–1540.

Hestholm, S.O. & Ruud, B.O., 1998. 3D finite difference elastic wave modelling including surface topography, *Geophysics,* **63,** 613–622.

Hestholm, S.O. & Ruud, B.O., 2000. 2D finite-difference viscoelastic wave modelling including surface topography, *Geophys. Prospect.,* **48,** 341–373.

Hoffman, K.A. & Chiang, S.T., 2000. *Computational Fluid Dynamics* (4th ed.), Engineering Education System, Wichita, Kansas.

Käser, M. & Igel, H., 2001. Numerical simulation of 2D wave propagation on unstructured grids using explicit differential operators, *Geophys. Prospect.,* **49,** 607–619.

Komatitsch, D., Coute, F. & Mora, P., 1996. Tensorial formulation of the wave equation for modelling curved interfaces, *Geophys. J. Int.,* **127,** 156–168.

Liu, X., Greenhalgh, S. & Wang, Y., 2011. 2.5-D poroelastic wave modelling in double porosity media, *Geophys. J. Int.,* **186,** 1285–1294.

Lombard, B., Piraux, J., Gelis, C. & Virieux, J., 2008. Free and smooth boundaries in 2-D finite-difference schemes for transient elastic waves, *Geophys. J. Int.,* **172,** 252–261.

Operto, S., Virieux, J., Dessa, J.X. & Pascal, G., 2006. Crustal seismic imaging from multifold ocean bottom seismometer data by frequency domain full waveform tomography: application to the eastern Nankai trough, *J. geophys. Res.,* **111,** B09306, doi:10.1029/2005JB003835.

Patantonis, D.E. & Atharassiadis, N.A., 1985. A numerical procedure for the generation of orthogonal body-fitted coordinate systems with direct determination of grid points on the boundary, *Int. J. Numer. Methods Fluids,* **5,** 245–255.

Pratt, R.G. & Shipp, R.M., 1999. Seismic waveform inversion in the frequency domain, part 2: fault delineation in sediments using crosshole data, *Geophysics,* **64,** 902–914.

Pratt, R.G. & Worthington, M.H., 1990. Inverse theory applied to multi-source crosshole tomography I: acoustic wave-equation method, *Geophys. Prospect.,* **38,** 287–310.

Pratt, R.G., Song, Z.M., Williamson, P. & Warner, M., 1996. Two-dimensional velocity models from wide-angle seismic data by wavefield inversion, *Geophys. J. Int.,* **124,** 323–340.

Ravaut, C., Operto, S., Improta, L., Virieux, J., Herrero, A. & Dell'Aversana, P., 2004. Multiscale imaging of complex structures from multifold wideaperture seismic data by frequency-domain full-waveform tomography: application to a thrust belt, *Geophys. J. Int.,* **159,** 1032–1056.

Tarantola, A., 2005. *Inverse Problem Theory and Methods for Model Parameter Estimation,* Soc. for Industrial & Applied Maths, Philadelphia.

Tarrass, I., Giraud, L. & Thore, P., 2011. New curvilinear scheme for elastic wave propagating in presence of curved topography, *Geophys. Prospect.,* **59,** 889–906.

Thomas, P.D. & Middlecoeff, J.F., 1980. Direct control of the grid point distribution in meshes generated by elliptic equations, *AIAA J.,* **18,** 652–656.

Thompson, J.F., Warsi, Z.U.A. & Mastin, C.W., 1985. *Numerical Grid Generation—Foundations and Applications,* North-Holland, New York.

Virieux, J., Calandra, H. & Plessix, R.E., 2011. A review of the spectral, pseudo-spectral, finite-difference and finite-element modelling techniques for geophysical imaging, *Geophys. Prospect.,* **59,** 794–813.

Wang, Y., 2011. Seismic waveform modeling and tomography, in *Encyclopedia of Solid Earth Geophysics,* pp. 1290–1301, ed. Gupta, H., Springer Verlag, Dordrecht.

Wang, Y. & Rao, Y., 2006. Crosshole seismic waveform tomography, I: strategy for real data application, *Geophys. J. Int.,* **166,** 1224–1236.

Wang, Y. & Rao, Y., 2009. Reflection seismic waveform tomography, *J. geophys. Res.,* **114,** B03304, doi:10.1029/2008JB005916.

Zhang, J., 2004. Wave propagation across fluid-solid interfaces: a grid method approach, *Geophys. J. Int.,* **159,** 240–252.

Zhang, J. & Gao, H., 2011. Irregular perfectly matched layers for 3D elastic wave modelling, *Geophysics,* **76,** T27–T36.

Zhang, J. & Liu, T., 1999. P-SV-wave propagation in heterogeneous media: grid method, *Geophys. J. Int.,* **136,** 431–438.

Zhang, W. & Chen, X., 2006. Traction image method for irregular free surface boundaries in finite difference seismic wave simulation, *Geophys. J. Int.,* **167,** 337–353.

APPENDIX A: A CONTROLLING TERM IN EQ. (6)

In seismic waveform simulation, we set $M(\varepsilon, \eta) = 0$ and evaluate $N(\varepsilon, \eta)$ in depth direction. Considering the second equation in Poisson's eq. (2), under the condition of orthogonality ($\beta = 0$), we obtain

$$\alpha \frac{\partial^2 z}{\partial \varepsilon^2} + \gamma \frac{\partial^2 z}{\partial \eta^2} = -J^2 N \dot{z}_\eta. \tag{A1}$$

Start from an equation with $N = 0$, as

$$\alpha \frac{\partial^2 z}{\partial \varepsilon^2} + \gamma \frac{\partial^2 z}{\partial \eta^2} = 0, \tag{A2}$$

and approximate it in finite-differencing as

$$\alpha(z_{i+1,j} - 2z_{i,j} + z_{i-1,j}) + \gamma(z_{i,j+1} - 2z_{i,j} + z_{i,j-1}) = 0. \tag{A3}$$

When $z_{i,j}$ has a perturbation dz, it can be written as

$$\alpha(z_{i+1,j} - 2(z_{i,j} + \mathrm{d}z) + z_{i-1,j}) + \gamma(z_{i,j+1} - 2(z_{i,j} + \mathrm{d}z) + z_{i,j-1}) = -J^2 N \dot{z}_\eta. \tag{A4}$$

This leads to the relationship between N and dz as

$$N = \frac{2(\alpha + \gamma)\mathrm{d}z}{J^2 \dot{z}_\eta}. \tag{A5}$$

Assuming $r = \frac{z_{i,j+1} - z_{i,j}}{z_{i,j} - z_{i,j-1}}$, it can also be expressed as

$$z_{i,j} = \frac{z_{i,j+1} + r z_{i,j-1}}{r + 1}. \tag{A6}$$

Downloaded from http://gji.oxfordjournals.org/ at Imperial College London Library on Ja 14

Perturbation dz at $z_{i,j}$ will cause a variation in r as

$$\mathrm{d}z = \frac{(z_{i,j-1} - z_{i,j+1})\mathrm{d}r}{(r+1)^2} = -\frac{L\,\mathrm{d}r}{(r+1)^2}, \tag{A7}$$

Then, eq. (A5) may be expressed as

$$N(\varepsilon, \eta) = -\frac{2L(\alpha+\gamma)\mathrm{d}r}{J^2(1+r)^2\dot{z}_\eta}. \tag{A8}$$

APPENDIX B: EXTENSION TO 3-D MODELS

The body-fitted grid method can also generate 3-D meshes for irregular topography, by adding another dimension in the eq. (1), as

$$\begin{cases} \dfrac{\partial^2\varepsilon}{\partial x^2} + \dfrac{\partial^2\varepsilon}{\partial y^2} + \dfrac{\partial^2\varepsilon}{\partial z^2} = M(\varepsilon, \zeta, \eta), \\ \dfrac{\partial^2\zeta}{\partial x^2} + \dfrac{\partial^2\zeta}{\partial y^2} + \dfrac{\partial^2\zeta}{\partial z^2} = L(\varepsilon, \zeta, \eta), \\ \dfrac{\partial^2\eta}{\partial x^2} + \dfrac{\partial^2\eta}{\partial y^2} + \dfrac{\partial^2\eta}{\partial z^2} = N(\varepsilon, \zeta, \eta), \end{cases} \tag{B1}$$

where (x, y, z) is the coordinate in the physical space, and $(\varepsilon, \zeta, \eta)$ is the coordinate in the computational space. The acoustic wave equation in the computational space may be extended to 3-D as

$$\begin{aligned} &\left(\dot{\varepsilon}_x^2 + \dot{\varepsilon}_y^2 + \dot{\varepsilon}_z^2\right)\frac{\partial^2 P}{\partial\varepsilon^2} + \left(\dot{\eta}_x^2 + \dot{\eta}_y^2 + \dot{\eta}_z^2\right)\frac{\partial^2 P}{\partial\eta^2} \\ &+ \left(\dot{\zeta}_x^2 + \dot{\zeta}_y^2 + \dot{\zeta}_z^2\right)\frac{\partial^2 P}{\partial\zeta^2} + 2\left(\dot{\varepsilon}_x\dot{\eta}_x + \dot{\varepsilon}_y\dot{\eta}_y + \dot{\varepsilon}_z\dot{\eta}_z\right)\frac{\partial^2 P}{\partial\varepsilon\partial\eta} \\ &+ 2\left(\dot{\varepsilon}_x\dot{\zeta}_x + \dot{\varepsilon}_y\dot{\zeta}_y + \dot{\varepsilon}_z\dot{\zeta}_z\right)\frac{\partial^2 P}{\partial\varepsilon\partial\zeta} \\ &+2\left(\dot{\eta}_x\dot{\zeta}_x + \dot{\eta}_y\dot{\zeta}_y + \dot{\eta}_z\dot{\zeta}_z\right)\frac{\partial^2 P}{\partial\eta\partial\zeta} \\ &+ \left(\ddot{\varepsilon}_{xx} + \ddot{\varepsilon}_{yy} + \ddot{\varepsilon}_{zz}\right)\frac{\partial P}{\partial\varepsilon} + \left(\ddot{\eta}_{xx} + \ddot{\eta}_{yy} + \ddot{\eta}_{zz}\right)\frac{\partial P}{\partial\eta} \\ &+ \left(\ddot{\zeta}_{xx} + \ddot{\zeta}_{yy} + \ddot{\zeta}_{zz}\right)\frac{\partial P}{\partial\zeta} + \frac{\omega^2}{v^2}P = 0. \end{aligned} \tag{B2}$$

Then both forward modelling and waveform inversion could be extended straightforwardly to 3-D geometry with curved topography.

Downloaded from http://gji.oxfordjournals.org/ at Imperial College London Library on January 17, 2014